29B X-721-67-145

END

NASA TM X- 55739

3 NOSE SELECTION AND VEHICLE MOTION DYNAMICS FOR THE SECOND STAGE OF A TWO-STAGE SOUNDING ROCKET SYSTEM 6

9 MARCH 1967 10

NASA — GODDARD SPACE FLIGHT CENTER

GREENBELT, MARYLAND 3

X-721-67-145

NOSE SELECTION AND VEHICLE MOTION DYNAMICS FOR THE SECOND STAGE OF A TWO-STAGE SOUNDING ROCKET SYSTEM

6 Edward E. Mayo
Mark B. Nolan 9 CV
Spacecraft Integration and
Sounding Rocket Division

March 1967

Goddard Space Flight Center
Greenbelt, Maryland

CONTENTS

ILLUSTRATIONS

TABLES

NOSE SELECTION AND VEHICLE MOTION DYNAMICS FOR THE SECOND STAGE OF A TWO-STAGE SOUNDING ROCKET SYSTEM

Edward E. Mayo
Mark B. Nolan
Goddard Space Flight Center
Greenbelt, Maryland

Abstract

Simple procedures are applied to the Nike-Tomahawk to arrive at an optimum nose shape which is utilized in subsequent aerodynamic and dynamic analyses. The effects of nose shapes on altitude performance, overall vehicle stability, and bending moments about the payload-rocket interface are discussed. The vehicle stability and undamped pitch frequencies are examined. A six-degree-of-freedom study is made of the vehicle dynamics at booster separation, at resonance, and after burnout. A comparison of Nicolaides' equilibrium solutions with vehicle dynamics at booster separation and at resonance shows that the solutions adequately predict the rolling trim. The vehicular motion constraints, level of aerodynamic pitch damping, and axial force contributions to the rolling trim at resonance are presented. The effects of payload weight, fin cant, fin misalignment, thrust misalignment and eccentricity, and level of aerodynamic pitch damping are each investigated. The allowable center-of-gravity offset (or induced rolling moment) to insure a break-out of roll "lock-in" was estimated by recently developed equilibrium equations, and was verified by dynamic simulation on a digital computer.

Symbols

a	Cylindrical afterbody
b	Body, (n + a)
c.v.	Center-of-volume
C_{N_α}	Normal force coefficient curve slope
C_{l_δ}	Roll forcing moment coefficient curve slope
C_{l_i}	Induced rolling moment coefficient
C_{l_p}	Roll damping coefficient, $\partial C_l / \partial \left(\frac{pd}{2V}\right)$
C_{m_α}	Static stability parameter
C_{m_q}	Pitch damping coefficient, $\partial C_m / \partial \left(\frac{qd}{2V}\right)$
d	Aerodynamic reference length, 0.75 ft.
$\boxed{1/2}_1$, $\boxed{1/2}_2$	Nutation and Precession arm half life
f_n	Nose fineness ratio
f_a	Afterbody fineness ratio
$\hat{f}_a$	Afterbody fineness ratio, from nose cylinder juncture to payload-rocket interface
(f+i)	Fins + interference
GPL	Gross payload
I	Pitch moment of inertia
I_A	Pitch moment of inertia about nose vertex
K_3	Rolling trim
K_{3_o}	Non-rolling trim
l	Distance from vehicle center-of-gravity to payload center-of-gravity
m	Bending moment at payload-rocket interface
n	Nose
p	Roll rate
p	Payload
q	Pitch rate
q	Dynamic pressure
r	Distance from payload rocket interface to payload center-of-gravity
S	Aerodynamic reference area, $\pi d^2/4$
S_W	Wetted surface area
t_2	Second stage ignition time
V	Vehicle velocity
V	Volume
W	Weight
$\bar{x}$	Longitudinal location, measured aft from nose vertex
$\bar{x}_{cg}$	Center of gravity location, measured aft from nose vertex
x_{cp}	Center of pressure location, measured forward from base

$\bar{x}_{cp}$	Center of pressure location, measured aft from nose vertex
z_t	Thrust eccentricity
ΔCG	Lateral center-of-gravity offset
δ	Fin cant angle
δ	Acute angle between axis of symmetry and tangent to outer surface, $\delta(\bar{x}/d)$
δ_f	Fin misalignment angle
ϵ	Thrust misalignment angle
ω	Undamped pitch frequency
ω_1, ω_2	Nutation and Precession arm rotation rates
λ_1, λ_2	Nutation and Precession arm damping rates
ρ	Body radius, $\rho(\bar{x}/d)$
σ	Density

Introduction

When an existing sounding rocket system is selected for the sounding rocket program, studies are performed to verify the flight worthiness of the vehicle in its existing configuration, establish payload weight and volume limitations, and define problem areas requiring special consideration.

This paper presents initial GSFC in-house efforts concerning nose optimization and vehicle motion dynamics for the Tomahawk upper stage of the Nike-Tomahawk system. The analysis was performed as the system was being placed in the NASA sounding rocket inventory.

Vehicle Description and Atmospheric Particle Trajectory

The Nike-Tomahawk system was developed by the Sandia Corporation for the U.S. Atomic Energy Commission. The system, shown with a representative payload in Figure 1, is a two stage, fin-stabilized vehicle that uses the Nike M5E1 motor for its booster and the Thiokol Tomahawk TE416 motor for its second stage. The main characteristics of the system are:

- Overall length 353 in.
- Weight (less gross payload):
  - lift-off 1860 lbs.
  - Nike burnout 1110 lbs.
- Nike motor:
  - burn duration 3.5 sec.
  - average sea level thrust 39,017 lbs.
  - total impulse 136,561 lb.-sec.
- Tomahawk upper stage:
  - length 206 in.
  - weight (less gross payload):
    - ignition 540 lbs.
    - burnout 143 lbs.
  - burn duration 9.5 sec.
  - average sea level thrust 9482 lbs.
  - total impulse 93,500 lb.-sec.
- Gross payload weight range 100 to 200 lbs.

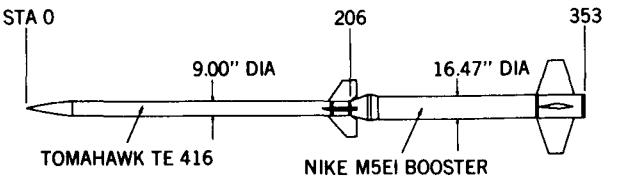

FIGURE 1. NIKE-TOMAHAWK SOUNDING ROCKET SYSTEM.

Figure 2 shows the atmospheric particle trajectory characteristics. The booster ignites at t=0 and burns for 3.5 seconds, at which time the booster separates. At this point the Mach number, dynamic pressure (q), and altitude are 2.3, 6200 lbs/ft^2, and 4500 ft., respectively. The Tomahawk coasts until 16 seconds, at which time ignition occurs. Pitch-roll coupling occurs near 20 seconds at M $\approx$ 4.0, q $\approx$ 5000 psf and altitude $\approx$ 37,000 feet. Burning continues until 25.5 seconds. The burnout Mach number is about 8 and the burnout altitude is about 68,000 feet. Minimum static margin occurs at Tomahawk burnout.

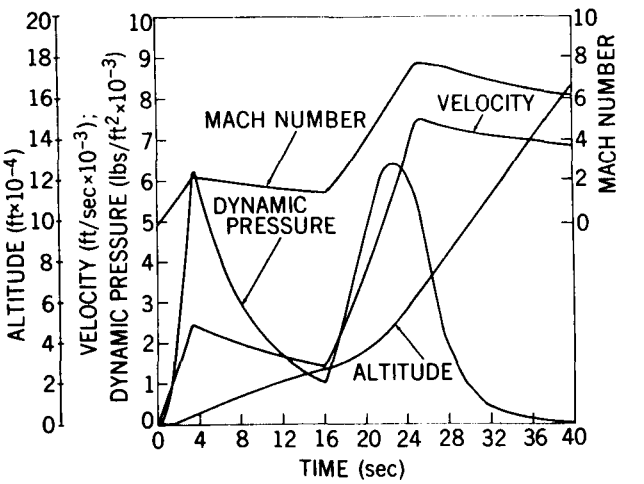

FIGURE 2. NIKE-TOMAHAWK ATMOSPHERIC PARTICLE TRAJECTORY. NOMINAL CONDITIONS.

Nose Selection

General

The nose selection method described is a simple approach which allows an intelligent choice of the optimum nose shape from the following considerations:

- Altitude performance
- Vehicle stability
- Payload-rocket interface bending moment

The nose shapes considered are ogives and cones having fineness ratios (f_n) of 3, 5, and 7.

Altitude Performance

The apogee comparison is obtained through the use of a particle trajectory program. This is accomplished by modifying the drag coefficient tables of the trajectory program according to the nose under investigation [1]. The results are presented in Table 1. In addition to the comparison of three tangent ogive and three conical noses, an investigation was made of two limiting conditions: a zero-drag nose, and a hemispherical nose (tangent ogive, $f_n = 0.5$). The difference in altitude between tangent ogive and conical noses of the same fineness ratio is only about 1 mile in 200 (1/2 percent). The maximum difference in apogee altitude is only 12 miles in 200 (6 percent), this being between an $f_n = 3$ ogive and $f_n = 7$ cone. All the conical and tangent ogive noses yielded apogee altitudes within 16 miles of the optimum (214.6 miles) given by the zero drag nose. The apogee altitude obtained with the hemisphere is very low (92.56 miles). The close grouping in apogee indicates that altitude performance will not be a major factor in the selection of the nose shape.

NOSE CONFIGURATION	APOGEE	
	STATUTE MILES	FEET
Ogive, $f_n = 3$	198.0	1,044,843
Ogive, $f_n = 5$	207.4	1,094,517
Ogive, $f_n = 7$	210.6	1,111,031
Cone, $f_n = 3$	199.9	1,054,911
Cone, $f_n = 5$	208.2	1,098,362
Cone, $f_n = 7$	210.8	1,111,942

LIMITING CASES:

NOSE CONFIGURATION	APOGEE	
	STATUTE MILES	FEET
Zero Drag Nose	214.3	1,130,512
Hemisphere (Ogive $f_n = 0.5$)	92.6	488,414

TABLE 1 - ALTITUDE PERFORMANCE FOR GROSS PAYLOAD WEIGHT = 123 POUNDS

Stability and Payload-Rocket Interface Bending Moments

Vehicle stability and payload-rocket interface bending moments are examined for two payload weight distribution cases (See Figure 3):

- Case I Uniform density payload contained within the payload cylindrical section (Figure 3 (a))
- Case II Constant volume and uniform density payload (Figure 3(b))

These two cases should bracket actual weight distributions. If the same conclusions can be drawn from these cases, they should also apply for the actual distribution. No efforts were made to smooth the aerodynamics used in obtaining the stability and payload-rocket interface bending moments. The payload geometric and mass characteristic equations are presented in Appendix A.

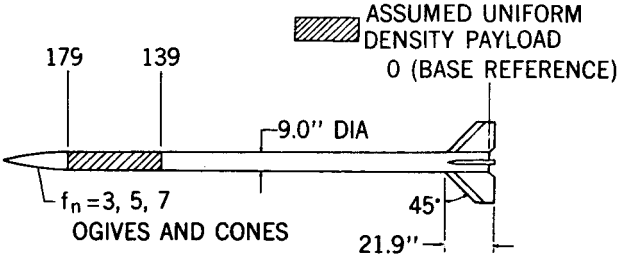

(a) PAYLOAD WEIGHT DISTRIBUTION CASE I.

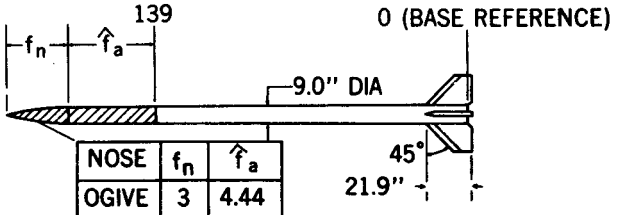

NOSE	f_n	$\hat{f}_a$
OGIVE	3	4.44
	5	3.37
	7	2.35
CONE	3	5.05
	5	4.41
	7	3.73

(b) PAYLOAD WEIGHT DISTRIBUTION CASE II.

FIGURE 3. TOMAHAWK TE416 SOUNDING ROCKET NOSE OPTIMIZATION STUDY MODELS. GPL = 123 POUNDS.

Stability. The stability characteristics of the various noses are determined by modifying existing Tomahawk ($f_n = 3$ ogive) wind tunnel data [2, 3]. The fin + interference characteristics are obtained by utilizing $f_n = 3$ ogive, $f_a = 10$ body experimental characteristics. [4] The fin + interference values are given by

$$C_{N_{\alpha(f+i)}} = C_{N_\alpha} - C_{N_{\alpha(n+a)}} \Big|_{\substack{f_n = 3 \text{ ogive} \\ f_a = 10}} \quad (1)$$

$$\left(x_{cp/d}\right)_{(f+i)} = \left\{ C_{N_\alpha}\left(x_{cp/d}\right) - \left[C_{N_{\alpha(n+a)}} \cdot \left(x_{cp/d}\right)_{(n+a)} \right]_{\substack{f_n = 3 \text{ ogive} \\ f_a = 10}} \right\} \Big/ C_{N_{\alpha(f+i)}} \quad (2)$$

The vehicle stability characteristics are then obtained by combining the fin + interference values with the body characteristics, i.e.,

$$C_{N_\alpha} = C_{N_\alpha}{}_{(f+i)} + C_{N_\alpha}{}_{(n+a)} \Big|_{f_a = 10} \quad (3)$$

$$x_{cp/d} = \left\{ C_{N_{\alpha(f+i)}} \left(x_{cp/d}\right)_{(f+i)} + \left[C_{N_{\alpha(n+a)}} \left(x_{cp/d}\right)_{(n+a)} \right]_{f_a=10} \right\} \Big/ C_{N_\alpha} . \quad (4)$$

The resulting stability characteristics, in terms of incremental static margin from the 3:1 ogive values, are presented in Figure 4. From Figure 4, the optimum nose shape depends on the Mach number of minimum stability. The Mach number of minimum stability for the Tomahawk is approximately 8. Therefore, the optimum nose shape from stability considerations is the $f_n = 3$ ogive. The only competitive shape is the 7:1 cone for payload weight distribution Case II; however, since the 7:1 cone's probable weight distribution is more accurately approximated by payload weight distribution Case I, the 3:1 ogive is considered the best shape.

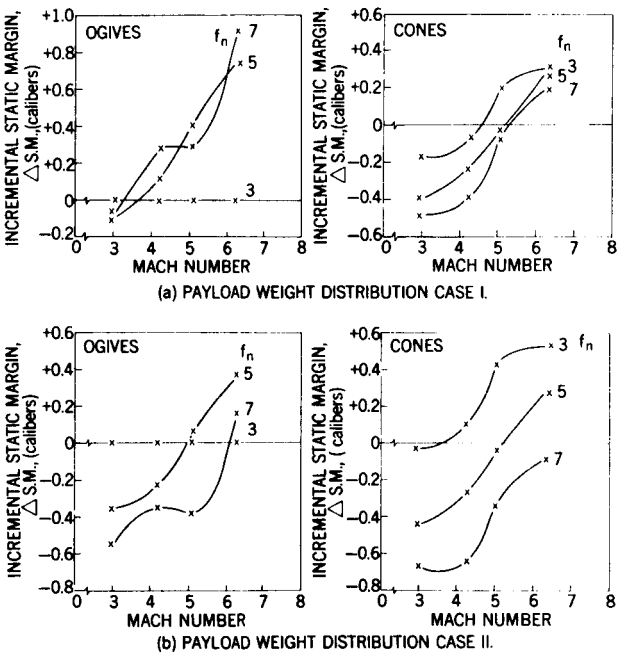

FIGURE 4. INCREMENTAL STATIC MARGIN FROM 3:1 OGIVES VALUES. (+ INDICATES DECREASED STABILITY).

Payload-Rocket Interface Bending Moments. The payload-rocket non-dimensionalized bending moments are assumed to be composed of aerodynamic, rotational inertial, and translational inertial components, i.e.:

$$\frac{m}{\alpha qSd} = \left|\frac{m}{\alpha qSd}\right| \text{ Aerodynamic} + \left|\frac{m}{\alpha qSd}\right| \text{ Rotational Inertial} - \left|\frac{m}{\alpha qSd}\right| \text{ Translational Inertial} \quad (5)$$

which may be expressed as,

$$\frac{m}{\alpha qSd} = C_{N_\alpha}{}_{b(f_n + \hat{f}_a)} \left[f_n + \hat{f}_a - \left(\frac{\bar{x}_{cp}}{d}\right)_{b(f_n + \hat{f}_a)} \right] - \frac{W_p l r}{32.2 I} C_{m_\alpha} - \frac{W_p}{W} C_{N_\alpha} \left[f_n + \hat{f}_a - \left(\frac{\bar{x}_{cg}}{d}\right)_p \right] \quad (6)$$

The resulting incremental non-dimensionalized bending moments from the $f_n = 3$ ogive values are shown in Figure 5. The Mach number of maximum dynamic pressure for the Tomahawk is approximately 6. Hence, the optimum nose shape depends upon the mass distribution of the payload. For uniform density payloads contained within the payload cylindrical section (payload weight distribution Case I), the $f_n = 3$ cone yields the lowest payload-rocket interface bending moment. For constant-volume, uniform-density payloads (payload weight distribution Case II), the fineness ratio 7 cone yields the lowest payload-rocket interface bending moments.

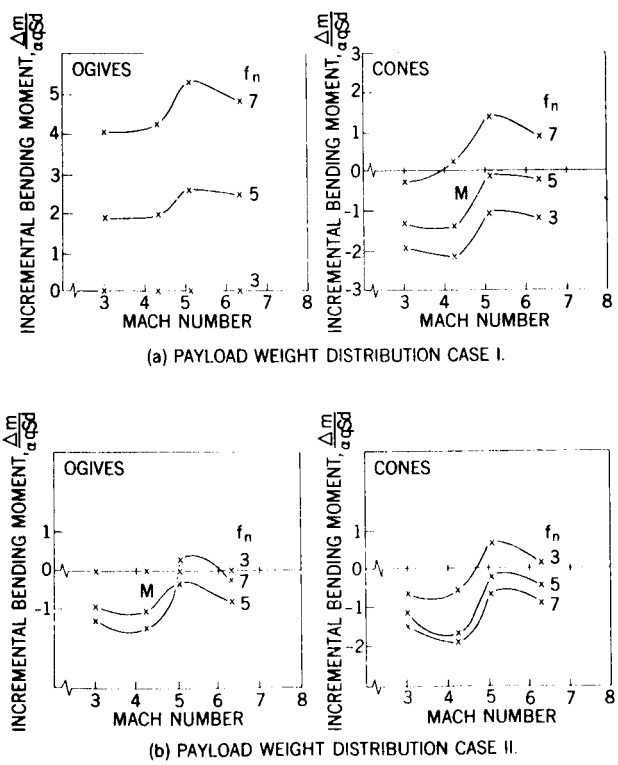

FIGURE 5. INCREMENTAL PAYLOAD-ROCKET INTERFACE NONDIMENSIONALIZED BENDING MOMENTS FROM 3:1 OGIVE VALUES. (+ INDICATES INCREASED MOMENTS).

Vehicle Motion Dynamic Analysis

Conditions

As a result of the nose optimization investigation, the $f_n = 3$ ogive (Figure 6) was selected for subsequent aerodynamic and dynamic analyses. From previous studies, the rigid body static stability was found to be insensitive to payload length for uniformly distributed, constant weight payloads. This stems from equal shifts in center-of-gravity and center-of-pressure associated with the length change. Hence, a nominal payload length was assumed.

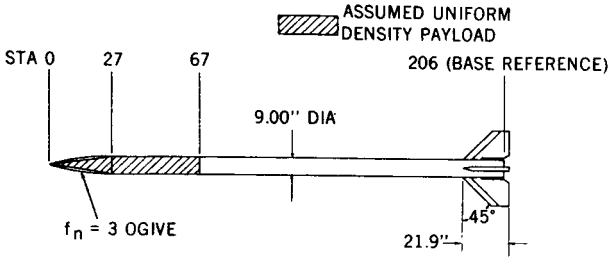

FIGURE 6. TOMAHAWK TE416 SOUNDING ROCKET DYNAMIC ANALYSIS STUDY MODEL.

Figure 7 shows the resulting stability and undamped pitch frequency. From stability considerations, a gross payload weight of around 80 pounds was determined as the minimum flyable payload weight. This weight corresponds to a maximum altitude of 224 statute miles or 360 kilometers (based on a nominal 80 degree launch angle). However, based on a recommended minimum static margin of 2 calibers, the maximum attainable altitude is about 200 statute miles. The undamped pitch frequency prior to resonance (Figure 7b) is insensitive to payload weight. From other calculations not presented herein, the static stability and natural frequency were found to be insensitive to launch angle.

The six-degree-of-freedom simulation time interval was from Nike booster burnout (t = 3.5 seconds) to approximately atmosphere exit time (t = 50 seconds). The initial conditions for position and velocity at 3.5 seconds were obtained from 80 degree sea level launch particle trajectory runs. The initial body orientation and body rates were assumed to be 4 degrees angle-of-attack and 720 degrees/second roll rate, respectively. A 0.2 degree angular thrust misalignment and 0.01 foot thrust eccentricity were assumed with the point of application at the base of the vehicle. A 0.2 degree fin misalignment and a fin center-of-pressure location 7 inches ahead of the base was assumed. The thrust and fin malalignments are consistent with those used in dispersion studies. The malalignments are always considered in the worst possible orientation.

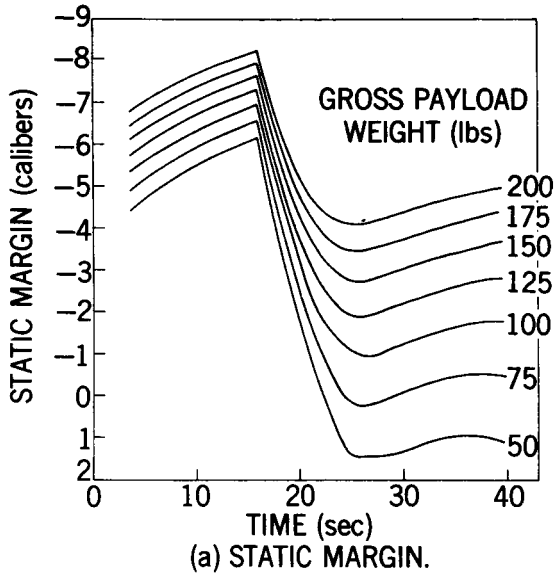

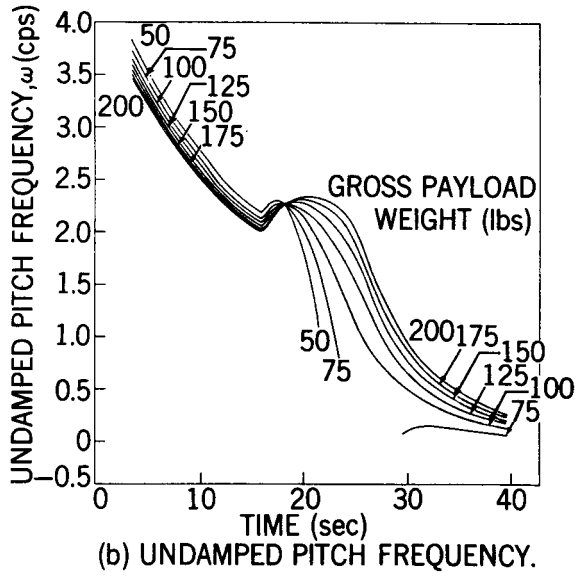

FIGURE 7. TOMAHAWK STATIC MARGIN AND UNDAMPED PITCH FREQUENCY CHARACTERISTICS.

Dynamics

Pitch-Roll Rates. The Tomahawk vehicle has four wedge-slab type fins which may be canted from 14' to 18' to produce the desirable roll history. For canted fins, the roll rate is proportional to the vehicle velocity. An examination of the Tomahawk velocity-time history will reveal that canted fins are desirable as roll producing devices. This stems from:

- Allowing the roll rate to remain safely below the pitch frequency during coast.
- A rapid increase in roll rate through resonance during which the roll forcing moment is much greater than the damping moment and adequate pitch damping exists.

- The large velocity increase during burning forces the roll rate to a safe distance above the undamped pitch frequency.

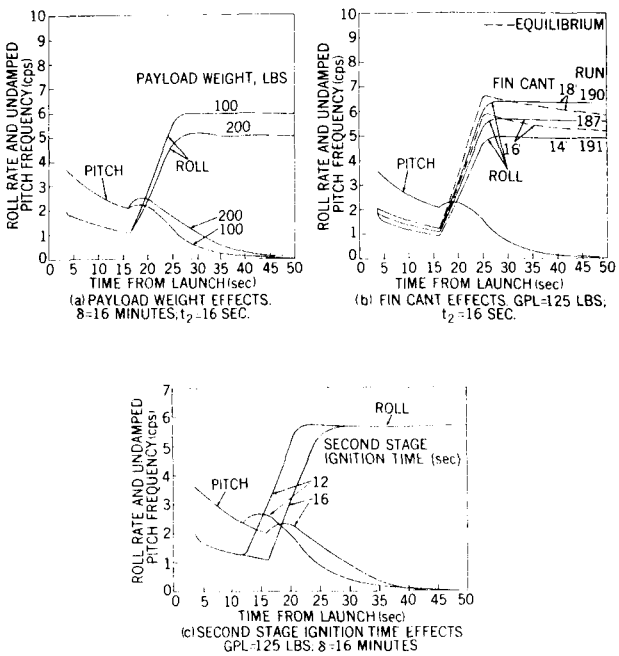

FIGURE 8. TOMAHAWK UNDAMPED PITCH RATE AND ROLL RATE HISTORIES.

The effects of gross payload weight, Tomahawk ignition time, and fin cant on the pitch-roll histories are contained in Figure 8. The primary effect of payload weight (Figure 8a) is the change in space roll rate which results from the change in burnout velocity. For the range of payload weights investigated (100 to 200 lbs.), the space roll rates are within 5.5 ± 0.5 cps. The effect of fin cant on the roll rate is given in Figure 8 (b). Also shown in Figure 8 (b) are equilibrium roll rates computed by $P_{ss} = -C_{l_\delta} \delta / [C_{l_p} (d/2V)]$. Initially, at t = 3.5 seconds, the actual roll rate is the assumed 2 cps initial condition. The roll rate reaches the steady state value within 0.2 second and remains at the steady state value until Tomahawk ignition. There is considerable lag during thrusting attributed to the high vehicle longitudinal acceleration coupled with roll inertia effects. After burnout, the actual roll rate overshoots the equilibrium value by approximately 0.5 cps at t = 50 seconds . The space roll rates are proportional to the fin cant, and the roll rate for all fin cants investigated is within 5.6 ± 0.75 cps. Figure 8 (c) shows that there is no effect of ignition time on final roll rate.

Booster Separation. The initial disturbance at booster separation damps from 4 degrees to 1 degree in approximately 1.1 seconds (See Figure 9). This is in agreement with the 0.57 Nutation and Precession Arm half life computed from equilibrium solutions[5]. The motion rapidly damps to the non-rolling trim value. Hence, the disturbances at booster separation are heavily damped and should not impose any serious flight abnormality.

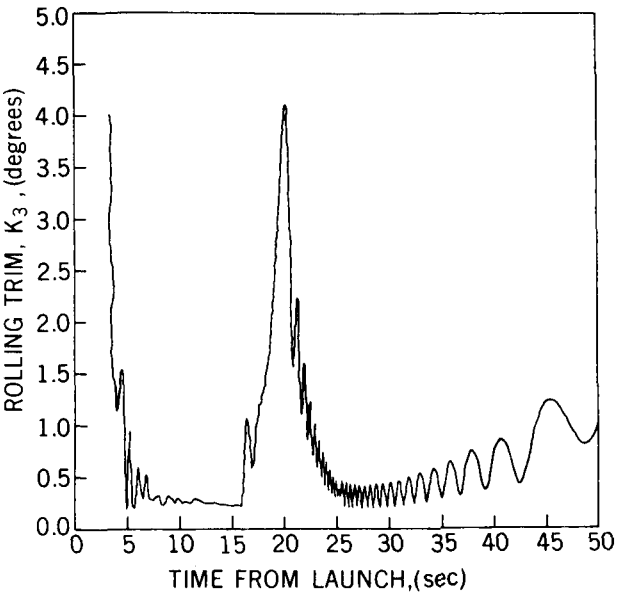

FIGURE 9. TOMAHAWK ROLLING TRIM HISTORY. GPL = 125 LBS; $\delta = 16'$; $\epsilon = 0.2^o$; $z_t = 0.01'$; $\delta_f = -0.2^o$

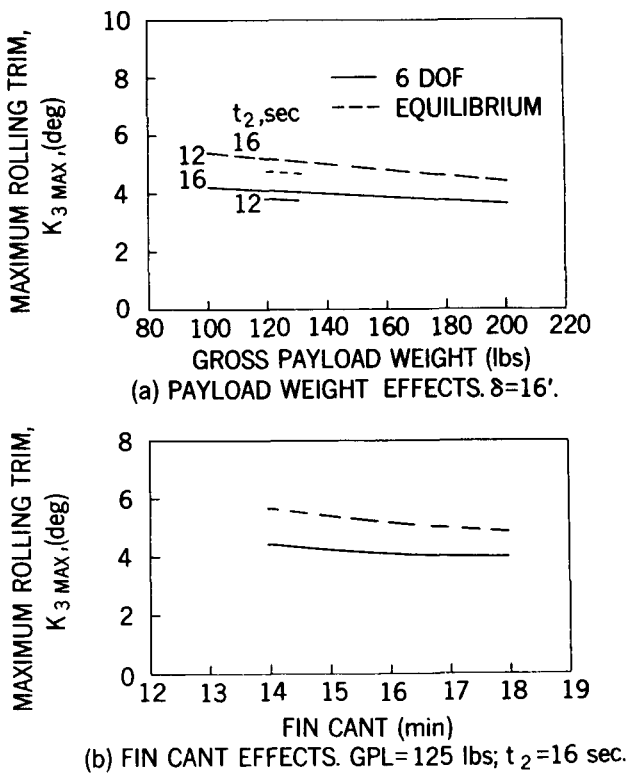

FIGURE 10. TOMAHAWK MAXIMUM ROLLING TRIM NEAR RESONANCE. $\epsilon = 0.2^o$, $z_t = 0.01'$, $\delta_f = -0.2^o$.

Resonance and Post Burnout. The effects of gross payload weight and fin cant on the dynamic and equilibrium rolling trim at resonance are presented in Figure 10. The maximum rolling trim is approxi-

mately 4 degrees and is within 1 degree of the equilibrium value[5]. Figure 10(a) shows that the effects of varying payload weight (and, thus, minimum static margin) have a relatively small effect on the rolling trim at resonance. This can be explained by referring to the static margins contained in Figure 7(a). The resonance time for the Tomahawk is approximately 20 seconds, while the minimum static margin occurs at burnout (25.5 seconds). In going from a gross payload weight of 200 lbs. to 100 lbs., the minimum static margin decreases from 4 calibers to 1 caliber; whereas, at resonance time, the static margin decreases from 5.25 to approximately 3.25 calibers. Similarly, for the case of zero minimum static margin, a static margin of over 2 calibers exists at the resonance time. The effect of varying fin cant on $(K_3)_{max}$ is presented in Figure 10(b). The small change in $(K_3)_{max}$ with varying fin cant is expected since the resonance time spread for extreme fin cants is only 1.25 seconds.

The effects of the various trim producing malalignments and aerodynamic parameters on the equilibrium trim at resonance were singularly investigated. The fin misalignment accounts for approximately 40 percent of $(K_3)_{max}$ at resonance, while the thrust malalignment accounts for the remaining 60 percent. The vehicular constraints, together with level of aerodynamic pitch damping and axial force contributions to the equilibrium resonance rolling trim are shown in Table II. From Table II and Figure 10, the rolling trim is adequately predicted by the equilibrium solutions if all vehicle motions are considered. The effect of level of aerodynamic pitch damping on the motion is given in Figure 11. Figure 11 shows that a 15 percent increase in $(K_3)_{max}$ occurs if C_{m_q} is assumed zero. This is considerably less than the 55 percent increase predicted from the equilibrium solutions (See Table II).

The level of aerodynamic pitch damping had a pronounced effect on the post burnout coning motion. The post burnout coning build-up serves only as an indication that the damping of the Nutation or Precession Arm may become sour. In this analysis, the Magnus term (which appears with C_{m_q} in determining the Nutation and Precession Arm damping rates) was neglected. Independent of its sign, the Magnus term damps one arm and undamps the other. The Magnus moment coefficients of the Tomahawk vehicle have been shown to be large, to be highly non-linear, and to vary rapidly with Reynolds number [6]. Hence, the degradation in damping due to decreasing density and aerodynamic coefficient degradation, coupled with post resonance residual motions, can result in large post burnout coning motions.

GPL = 125 lbs; t_2 = 16 sec; δ = 16'; ϵ = 0.2°; z_t = .01'; δ_f = −0.2°.

MOTION	p (rad/sec)	ω_1 (rad/sec)	ω_2 (rad/sec)	λ_1 (1/sec)	λ_2 (1/sec)	$(\frac{1}{2})_1$ (sec)	$(\frac{1}{2})_2$ (sec)	K_{3_o} (deg)	$\frac{K_3}{K_{3_o}}$	K_3 (deg)
P & Y	14.89	14.43	-14.33	-0.37	-0.37	1.86	1.87	0.60	18.95	11.37
P, Y, H & S_W	14.89	14.43	-14.33	-0.60	-0.60	1.15	1.15	0.60	11.75	7.05
P, Y, H, S_W & S_u	14.89	14.43	-14.33	-0.82	-0.82	0.85	0.85	0.60	8.67	5.20
P, Y, H, S_W, S_u, & C_{m_q} = 0	14.89	14.43	-14.33	-0.53	-0.53	1.32	1.32	0.60	13.47	8.08
P, Y, H, S_W, S_u, & C_X = 0	14.89	14.43	-14.33	-0.83	-0.83	0.83	0.83	0.60	8.49	5.09

WHERE P & Y — PITCHING AND YAWING
P, Y, H, S_W — PITCHING, YAWING, HEAVING AND SWERVING
P, Y, H, S_W, S_u — PITCHING, YAWING, HEAVING, SWERVING AND SURGING

TABLE 2 – EQUILIBRIUM RESONANCE CHARACTERISTICS

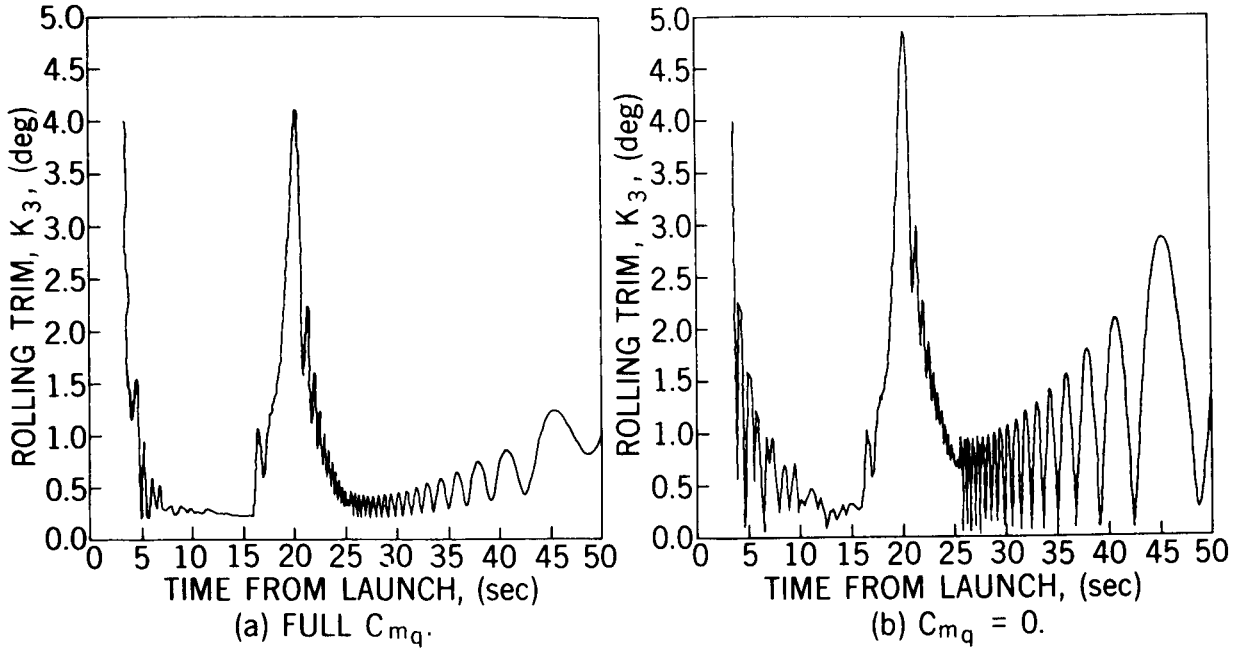

FIGURE 11. TOMAHAWK ROLLING TRIM HISTORY. GPL = 125 LBS.
$\delta = 16'$; $\epsilon = 0.2^{\circ}$; $z_t = 0.01'$; $\delta_f = -0.2^{\circ}$.

Lateral Center-of-Gravity Offset Limit. As noted previously, the rolling trim at resonance is in agreement with equilibrium values predicted by resonance instability theory. Thus, $(K_3)_{max}$ can be estimated by equilibrium procedures[5]. As seen from Figure 12(a), the Nutation and Precession Arm damping rates after burnout decrease exponentially with time (Figure 12 is for full estimated C_{m_q}). The decreased damping is reflected in $(K_3)_{max}$ versus time (Figure 12(b)). Figure 12(b) illustrates that if "lock-in" occurs, $(K_3)_{max}$ will grow exponentially. It is interesting to note that at t = 24 seconds the thrust misalignment accounts for 53% of the non-rolling trim. However, owing to loss in jet damping and axial acceleration, the rolling trim decreases only 20% at thrust termination. (In some sounding rocket systems a step increase in rolling trim occurs at thrust termination.)

The allowable center-of-gravity offset (or induced rolling moment) to insure a break-out of "lock-in" was estimated by recently developed equilibrium equations[7]. Considering Δ CG = 0 then the induced rolling moment required to maintain "lock-in" may be approximated by:

$$-C_{l_i} = \delta C_{l_\delta} + C_{l_p}\left(\frac{\omega d}{2V}\right) . \qquad (7)$$

The resulting C_{l_i} values are given in Figure 13(a) as a

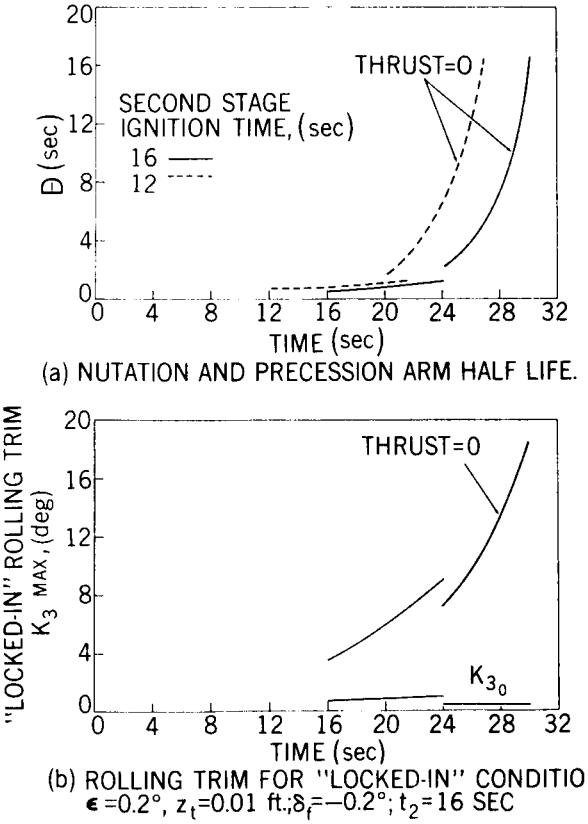

FIGURE 12. EQUILIBRIUM DAMPING AND "LOCKED-IN" ROLLING TRIM GPL = 125 LBS.

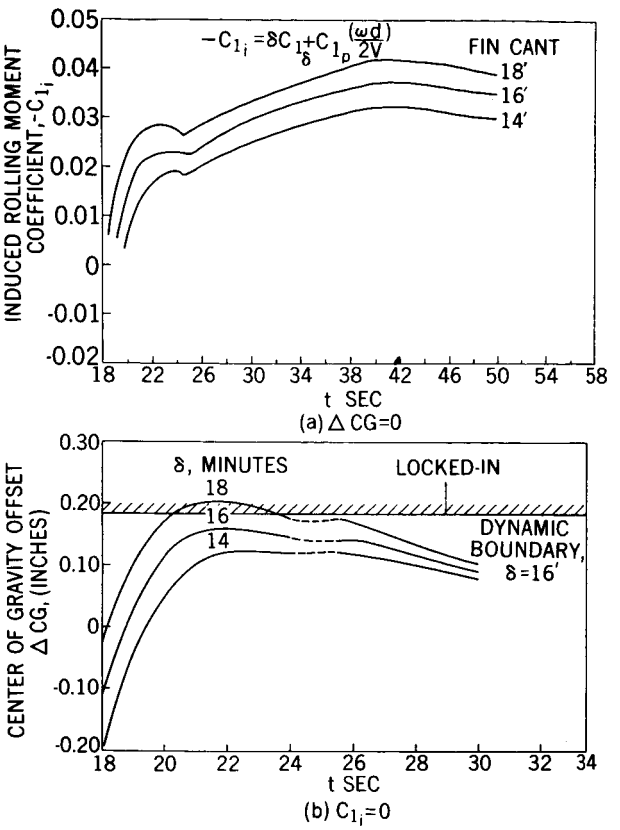

FIGURE 13. MAGNITUDE OF INDUCED ROLLING MOMENT OR CENTER-OF-GRAVITY OFFSET REQUIRED TO SUSTAIN "LOCK-IN" CONDITION.
GPL = 125 LBS; $\epsilon = 0.2^o$; $z_t = 0.01$ ft.; $\delta_f = -0.2^o$.

function of time and fin cant angle. Figure 13(a) is interpreted as follows. If an induced rolling moment of -0.015 exists, then for δ = 16' roll "lock-in" will be maintained until break-out occurs at 20 seconds ($(K_3)_{max} \approx 6$ degrees from Figure 12(b)). If, for the same cant angle, an induced rolling moment coefficient of -0.030 exists, then roll lock-in will be maintained until break-out occurs at 30.5 seconds ($(K_3)_{max} \approx 20$ degrees, from Figure 12(b)). From equation (7) and Figure 13(a), the allowable induced rolling moment is a direct function of the fin cant.

Considering $C_{l_i} = 0$ and the worst center-of-gravity and fin misalignment orientation, the allowable center-of-gravity offset may be approximated by:

$$\Delta CG = \frac{12d}{C_{N_\alpha} (K_3)_{max}} \left[\delta C_{l_\delta} + C_{l_p} \left(\frac{\omega d}{2V}\right)\right] \qquad (8)$$

The resulting ΔCG values are given in Figure 13(b) as a function of time and fin cant angle. Figure 13(b) is interpreted similar to Figure 13(a). For δ = 16 minutes, a center-of-gravity offset greater than 0.165 inch can prevent break-out from lock-in. For ΔCG = 0.11 inches, however, break-out occurs at t = 20 sec. ($(K_3)_{max} \approx 6$ degrees, from Figure 12(b)). From equation (8) and Figure 13(b), the allowable center-of-gravity offset is a direct function of the fin cant angle. As expected, the equilibrium values are in agreement and slightly conservative when compared with dynamic simulations.

Conclusions

Summarized Significant Conclusions

1. The difference in apogee altitude between the f_n = 3 ogive and f_n = 7 cone is only 12 miles in 200 (6%).

2. The optimum nose shape from stability considerations is the f_n = 3 ogive.

3. The optimum nose shape from payload-rocket interface bending moment considerations depends upon the mass distribution of the payload. For uniform density payloads contained within the payload cylindrical section, the f_n = 3 cone yields the lowest payload-rocket interface bending moment. For constant volume-uniform density payloads, however, the fineness ratio 7 cone yields the lowest payload-rocket interface bending moment.

4. From stability considerations, a gross payload weight of around 80 pounds is the minimum flyable payload weight. Based on a nominal 80-degree launch angle, this weight corresponds to a maximum altitude of 224 statute miles or 360 kilometers. However, based on the recommended minimum static margin of 2 calibers, the maximum attainable altitude is about 200 statute miles.

5. From consideration of the vehicle's inherent velocity-time history, the canted fin roll control design appears attractive.

6. The undamped pitch frequency prior to resonance is insensitive to payload weight.

7. The space roll rates for all payload weights and fin cants investigated are within 5.6 ± 0.75 cps.

8. The disturbances at booster separation are heavily damped and should not impose any serious flight abnormality.

9. The maximum rolling trim near resonance is approximately 4 degrees, within 1 degree of the equilibrium value, and insensitive to payload weight and fin cant.

10. Fin misalignments account for approximately 40 percent of the combined angle-of-attack at resonance while thrust malalignments account for the remaining 60 percent. (Only fin and thrust malalignments were considered.)

11. The pre-burnout combined angle-of-attack is insensitive to the level of aerodynamic pitch damping.

12. The degradation in damping due to decreasing density and aerodynamic coefficient degradation, coupled with post resonance residual motions, can result in large post burnout coning motions.

13. Considering fin cant, $\delta = 16$ minutes, an induced rolling moment coefficient, C_{l_i} of -0.0375, or a center-of-gravity offset, ΔCG, greater than 0.165 inches can prevent breakout from roll "lock-in".

References

1. Morris, Deane N., "A Summary of the Supersonic Pressure Drag of Bodies of Revolution," J. A. S. (July 1961).

2. Connell, G. M., "Wind-Tunnel Force Tests of Five Tomahawk Models at Mach 5 and Mach 7.5," Sandia Corporation TM 355-63(74) (January 1964).

3. Connell, G. M., "Trisonic Wind-Tunnel Force Tests of Tomahawk Models," (December 1963).

4. Syverston, C. A. and Dennis, D. H., "A Second-Order Shock-Expansion Method Applicable to Bodies of Revolution Near Zero Lift," NACA Report 1328 (1957).

5. Nicolaides, J. D., "Missile Flight and Astrodynamics," Bureau of Naval Weapons Technical Note 100A (1961).

6. Stone, G. W., "The Magnus Instability of a Sounding Rocket," Paper No. 66-62, AIAA 3rd Aerospace Sciences Meeting, New York (January 24-26, 1966).

7. Price, D. A. and Nelson, E. O., "Final Report for Aerobee 350 Roll Lock-In Study," LMSC, Palo Alto, California (1965).

Appendix A

Presented here are the non-dimensionalized expressions for the geometric and mass characteristics of uniform density ogive-cylinder and cone-cylinder payloads. The evaluation of the ogive nose expressions requires double precision to meet accuracy requirements.

Nose Equations

Ogive. The ogive equations may be expressed as:

$$\rho/d = \sqrt{(f_n^2 + 1/4)^2 - (\bar{x}/d - f_n)^2} - (f_n^2 - 1/4)$$

$$\delta = \tan^{-1}\left[\frac{f_n - \bar{x}/d}{\rho/d + f_n^2 - 1/4}\right]$$

$$\frac{V_n}{\pi d^3} = f_n (f_n^2 + 1/4)^2 - 1/3\, f_n^3 - (f_n^2 - 1/4)(f_n^2 + 1/4)^2 \sin^{-1}\left(\frac{f_n}{f_n^2 + 1/4}\right)$$

$$(c.v./d)_n \frac{V_n}{\pi d^3} = 1/2\, f_n^2 (f_n^2 + 1/4)^2 - 1/12\, f_n^4 - 2(f_n^2 - 1/4)(f_n^2 + 1/4)^2 \left[1/2\, f_n \sin^{-1}\left(\frac{f_n}{f_n^2 + 1/4}\right) - 1/3\,(f_n^2 + 1/4)\right]$$
$$+ 2(f_n^2 - 1/4)^2 \left[-\frac{(f_n^2 - 1/4)^2}{3} - \frac{f_n^2}{2}\right] + 1/2\, f_n^2 (f_n^2 - 1/4)^2$$

$$\left(\frac{I_A}{\sigma \pi d^5}\right)_n = \int_0^{f_n} (\bar{x}/d)^2 \, (\rho/d)^2 \, d(\bar{x}/d) = 1/3\, f_n^3 (f_n^2 + 1/4)^2 - 1/30\, f_n^5 + 4/3\, f_n (f_n^2 + 1/4)^3 (f_n^2 - 1/4)$$

$$-5/6\, f_n (f_n^2 - 1/4)^4 - \left[5/4\, f_n^2 (f_n^2 - 1/4) + 1/4\, (f_n^2 - 1/4)^3\right]$$

$$\left[f_n (f_n^2 - 1/4) + (f_n^2 + 1/4)^2 \sin^{-1}\left(\frac{f_n}{f_n^2 + 1/4}\right)\right] + 1/3\, f_n^3 (f_n^2 - 1/4)^2$$

$$\left(\frac{S_W}{S}\right)_n = 8 (f_n^2 + 1/4)^2 \left\{\sin\left[\tan^{-1}\left(\frac{f_n}{f_n^2 - 1/4}\right)\right] - \left(1 - \frac{1}{2f_n^2 + 0.5}\right) \tan^{-1}\left(\frac{f_n}{f_n^2 - 1/4}\right)\right\}$$

Cone. The cone equations may be expressed as:

$$\frac{V_n}{\pi d^3} = (1/12)\, f_n$$

$$(c.v./d)_n = .75\, f_n$$

$$\left(\frac{I_A}{\sigma \pi d^5}\right)_n = .05\, f_n (1/16 + f_n^2)$$

$$\left(\frac{S_W}{S}\right)_n = \sqrt{1 + 4 f_n^2}$$

Cylindrical Afterbody Equations

The afterbody equations are:

$$\frac{V_a}{\pi d^3} = (1/4)\, \hat{f}_a$$

$$\left(\frac{c.v.}{d}\right)_a = f_n + \hat{f}_a/2$$

$$\frac{I_a}{\sigma \pi d^5} = 1/16\, \hat{f}_a \left[0.25 + \frac{\hat{f}_a^2}{3}\right]$$

Payload Equations

The payload equations are:

$$\frac{V_p}{\pi d^3} = \frac{V_n}{\pi d^3} + \frac{V_a}{\pi d^3}$$

$$(c.v./d)_p = \frac{\frac{V_n}{\pi d^3}(c.v./d)_n + \frac{V_a}{\pi d^3}(c.v./d)_a}{V_p / \pi d^3}$$

$$\left(\frac{I}{\sigma \pi d^5}\right)_p = \left(\frac{I_A}{\sigma \pi d^5}\right)_n - \frac{V_n}{\pi d^3}\left[\left(\frac{c.v.}{d}\right)_n\right]^2 + \frac{V_n}{\pi d^3}\left[\left(\frac{c.v.}{d}\right)_p - \left(\frac{c.v.}{d}\right)_n\right]^2 + \frac{I_a}{\sigma \pi d^5} + \frac{V_a}{\pi d^3}\left[\left(\frac{c.v.}{d}\right)_a - \left(\frac{c.v.}{d}\right)_p\right]^2$$

$$(S_W/S)_p = \left(\frac{S_W}{S}\right)_n + \left(\frac{S_W}{S}\right)_a$$